Applied Physics A (2022) 128:168
https://doi.org/10.1007/s00339-022-05281-x

Applied Physics A
Materials Science & Processing

Magnetic properties of new (1−x)$Bi_{1/2}Na_{1/2}TiO_3$+x$BaNiO_{3-\delta}$ solid solution materials

Dang Duc Dung[1] · Nguyen Hoang Thoan[1] · Phan Van Vinh[2] · Nguyen Huu Lam[1] · Vu Tien Lam[1] · Pham Dinh Luong[1] · Duong Quoc Van[2] · Dorj Odkhuu[3]

Received: 4 December 2021 / Accepted: 8 January 2022 / Published online: 1 February 2022

Abstract

New solid solution (1−x)$Bi_{1/2}Na_{1/2}TiO_3$+x$BaNiO_{3-\delta}$ materials were synthesized by a chemical method. The X-ray diffraction and Raman scattering structure studies confirmed that the $BaNiO_{3-\delta}$ materials were well soluted in the host $Bi_{1/2}Na_{1/2}TiO_3$ materials. The random incorporation of Ba and Ni into the host $Bi_{1/2}Na_{1/2}TiO_3$ materials was displayed by the optical properties where the optical bandgap values were reduced, and the photoluminescence was suppressed. The complex magnetic properties of $Bi_{1/2}Na_{1/2}TiO_3$ materials were obtained as a function of $BaNiO_{3-\delta}$ amounts in the solid solutions. The role of co-modification of *A*- and *B*-sites via alkaline earth metals and transition metals as substitution and interstitially on magnetic properties of $Bi_{1/2}Na_{1/2}TiO_3$ materials was experimentally proposed, which is further supported by first-principles density functional theory calculations. We expected that our work provided a new method to inject the ferromagnetic properties in lead-free ferroelectric materials for smart electronic applications.

Keywords $Bi_{1/2}Na_{1/2}TiO_3$ · $BaNiO_{3-\delta}$ · Sol–gel · Lead-free ferroelectric · Ferromagnetism

1 Introduction

Advanced functional materials had been promised for use in smart electronic devices [1–3]. Among them, the lead-free ferroelectric materials tailored with ferromagnetic properties were candidates for extending the function materials in electronic devices, such as using the magnetic field controlling the electrical polarization and electrical field tuning the magnetization [3]. Recently, lead-free ferroelectric $Bi_{1/2}Na_{1/2}TiO_3$-based materials were rapidly developed because they are friendly to human health and non-toxic to the environment in comparison with traditional ferroelectric $Pb(Zr,Ti)O_3$-based materials [4]. The lead-free ferroelectric $Bi_{1/2}Na_{1/2}TiO_3$ materials, first synthesized by Smolensky et al. exhibited good electrical properties [5]. Recently, the observation of room temperature ferromagnetism in $Bi_{1/2}Na_{1/2}TiO_3$ materials via self-defect such of Na-, Bi- or Ti-vacancies was very important to promise for extension the function materials in electronic devices [6, 7]. However, the materials had low magnetization at room temperature, normally about 1–2 memu/g, which hindered the transfer of their materials into electronic devices [6–12]. Therefore, magnetic property enhancement for $Bi_{1/2}Na_{1/2}TiO_3$-based materials was an important challenge for the development of multiferroic materials based on lead-free ferroelectric materials.

In fact, the magnetic properties of the $Bi_{1/2}Na_{1/2}TiO_3$ materials had been improved by the use of transition metal impurities (e.g., Fe, Co, Ni, Mn, and Cr) [8–12]. Thanh et al. reported that the improved magnetic performance at room temperature might rise from oxygen vacancies (□) and be promoted via magnetic pair $Mn^{2+/3+}$-□-$Mn^{2+/3+}$ [8, 9]. Dung et al. reported that the Co-, Ni- and Fe-doped $Bi_{1/2}Na_{1/2}TiO_3$ materials exhibited the room temperature

✉ Dang Duc Dung
dung.dangduc@hust.edu.vn

Duong Quoc Van
vandq@hnue.edu.vn

Dorj Odkhuu
odkhuu@inu.ac.kr

[1] School of Engineering Physics and Multifunctional Ferroics Materials Lab., Ha Noi University of Science and Technology, 1 Dai Co Viet Road, Ha Noi, Viet Nam

[2] Faculty of Physics, Ha Noi National University of Education, 136 Xuan Thuy, Ha Noi, Viet Nam

[3] Department of Physics, Incheon National University, Incheon 22012, South Korea

ferromagnetism via most original from the interactions of Co, Ni and Fe cations through oxygen vacancies, e.g., $Co^{2+/3+}$-□-$Co^{2+/3+}$, $Ni^{2+/3+}$-□-$Ni^{2+/3+}$ or $Fe^{2+/3+}$-□-$Fe^{2+/3+}$ [10–12]. However, due to the limitation of transition metal cations in elements predictable that hinted the extension in research to advance the magnetic performance of lead-free ferroelectric $Bi_{1/2}Na_{1/2}TiO_3$ materials. Thanks to well solid solute with various types of ABO_3-based materials, the ferromagnetism ordering at room temperature in ABO_3-modified $Bi_{1/2}Na_{1/2}TiO_3$ materials was obtained [13–24]. We recently proved the new method to advance the magnetic properties of $Bi_{1/2}Na_{1/2}TiO_3$ materials via using the *A*-site vacancies together with magnetic pairs of transition metal interaction through oxygen vacancies [13–16]. In addition, the complex co-modification of *A*-site via alkaline earth cation and *B*-site via transition metal of host $Bi_{1/2}Na_{1/2}TiO_3$ materials was also exhibited a strong enhancement in the magnetization [7, 17–24].

Among alkaline earth nickelates, $BaNiO_{3-\delta}$ materials exhibited various structures as a function of the valence state of Ni and oxygen deficiency [25–28]. Lee et al. reported that hexagonal perovskite $BaNiO_3$ materials exhibited unusual high valence nickel (IV) [25]. Gottschall et al. showed that the $BaNiO_3$ materials have trivalent Ni and oxygen anion holes which possibly corresponded to $Ba^{2+}Ni^{3+}(O^{2})_2O^{\bullet-}$ [26]. Lopez et al. reported the phase transition from $BaNiO_3$ to $BaNiO_2$ via valence state changing the cause of Ba were deficiencies [27]. Lander et al. reported that $Ba_2Ni_2O_5$ materials had a hexagonal structure, while $BaNiO_3$ exhibited a cubic structure [28]. However, so far, there was still no information about the $BaNiO_{3-\delta}$-modified $Bi_{1/2}Na_{1/2}TiO_3$ compounds as solid solutions.

In this work, the $(1-x)Bi_{1/2}Na_{1/2}TiO_3+xBaNiO_{3-\delta}$ materials were synthesized by the simple chemical method and studied with the density functional theory (DFT) calculations. The $BaNiO_{3-\delta}$ materials were found to well solid solute into $Bi_{1/2}Na_{1/2}TiO_3$ materials which resulted in random incorporation of Ba and Ni cations into the host $Bi_{1/2}Na_{1/2}TiO_3$ materials. The presentation of Ba and Ni in the host lattices resulted in complex optical band gap energy and magnetic properties of host $Bi_{1/2}Na_{1/2}TiO_3$ materials. The underlying mechanism for the substitution-induced ferromagnetism has been discussed with the DFT electronic structure.

2 Experimental

In this study, pure $Bi_{1/2}Na_{1/2}TiO_3$ and $(1-x)Bi_{1/2}Na_{1/2}TiO_3+xBaNiO_{3-\delta}$ materials (named BNT pure and BNT-$xBaNiO_{3-\delta}$, x = 0.5; 1; 3; 5; 7 and 9 mol.%, respectively) were prepared by a chemical route method. The raw materials consisted of bismuth nitrate pentahydrate ($Bi(NO_3)_3.6H_2O$), sodium nitrate ($NaNO_3$), barium carbonate ($BaCO_3$), nickel nitrate ($Ni(NO_3)_2.6H_2O$), and tetraisopropoxytitanium(IV) ($C_{12}H_{28}O_4Ti$). The chemical legends in our experiment were acetylacetone ($CH_3COCH_2COCH_3$) and acid acetic (CH_3COOH). Firstly, $BaCO_3$ was weighed and dissolved in a solution of acid acetic in de-ion water. Secondly, the $Bi(NO_3)_3.6H_2O$ was weighed and added to the solution. The solution was kept under magnetic stirring until turning transparent. Subsequently, $NaNO_3$ and $Ni(NO_3)_2.6H_2O$ were weighted and added to the homogeneous solution. Before dropping $C_{12}H_{28}O_4Ti$ into the solution, acetylacetone was added to prevent hydroxylation of Ti^{4+} cations. The final solution was kept in magnetic stirring for several hours until turning light blue transparent. The dry gels were formed via heating the sol under 100 °C. The powders were fabricated by annealing dry gel under 800 °C for 3 h in the air. Sodium (Na) is a light element and easy to evaporate from sols that make the samples non-stoichiometric. Thus, the sodium loss was prevented by weighting an extra Na amount of about 30% from the initial $NaNO_3$ source [7, 24]. The presence of chemical elements and chemical mapping in the studied samples was characterized by energy-dispersive X-ray spectroscopy (EDX, S-4800 Hitachi) and further confirmed the composition by electron probe microanalysis (EPMA, Shimadzu EPMA 1600). The crystal structure was performed by X-ray diffraction (XRD, Brucker D8 Advance). The phonon vibration modes of samples were carried by Raman scattering with a 473 nm LASOS laser and a DU420A-Oe defector. The optical properties of samples were studied by Ultraviolet–Visible (UV–Vis, Jasco V-670) and photoluminescence (PL, exciter with 473 nm LASOS laser and a DU420A-Oe defector), spectroscopy. The magnetic properties of samples were characterized by a Vibrating Sample Magnetometer (VSM, Lakeshore 7404). All measurements were performed at room temperature.

3 Results and discussion

Figure 1a and b showed EDX spectra of the pure BNT and BNT-$5BaNiO_{3-\delta}$ samples, respectively. The inset of each figure showed the area chosen for chemical indexing. As shown in Fig. 1a, the EDX spectrum of the pure BNT material exhibited the presence of all expected chemical elements, including Bi, Na, Ti, and O. The addition of typical Ni and Ba peaks in the EDX spectrum of BNT-$5BaNiO_{3-\delta}$ material, as shown in Fig. 1b, provided solid evidence for the presence of impurity elements in the studied samples. The chemical composition of a studied sample was further confirmed by EPMA methods, as mentioned in the experimental part.

The distribution of impurity elements in the BNT-$5BaNiO_{3-\delta}$ sample is shown in Fig. 2. The surface morphology of a selected area for chemical mapping is shown in

Fig. 2a, whereas Fig. 2b–g presented chemical mappings of Bi, Na, Ti, O, Ba and Ni elements, respectively. The results indicated that both the host and impurity elements were homogeneously dispersed in the sample.

The influence of $BaNiO_{3-\delta}$ phase on the crystal structure of the host $Bi_{1/2}Na_{1/2}TiO_3$ materials is shown in Fig. 3a, where the XRD patterns were plotted for the pure $Bi_{1/2}Na_{1/2}TiO_3$ and $BaNiO_{3-\delta}$-modified $Bi_{1/2}Na_{1/2}TiO_3$ materials with various $BaNiO_{3-\delta}$ amounts. The XRD pattern of the pure $Bi_{1/2}Na_{1/2}TiO_3$ was well indexed as rhombohedral symmetry (JCPDS card no. 00-036-0340, space group R3c) with a polycrystalline structure by considering the XRD peak positions and their relative intensity. Our results were well consistent with recent reports on the rhombohedral perovskite-type crystal structure of chemically synthesized $Bi_{1/2}Na_{1/2}TiO_3$ materials [7–24]. No impurity phase or phase segregation was detected by the X-ray diffraction patterns. The number of the XRD peaks of the $Bi_{1/2}Na_{1/2}TiO_3$ materials was unchanged with the addition of the $BaNiO_{3-\delta}$ compound. In addition, no extra peak was observed in the XRD patterns as increasing $BaNiO_{3-\delta}$ concentrations in $Bi_{1/2}Na_{1/2}TiO_3$ materials. The results were suggested that the $BaNiO_{3-\delta}$ materials were well dissolved in the host $Bi_{1/2}Na_{1/2}TiO_3$ lattices, leading to random incorporation of Ba and Ni into the host $Bi_{1/2}Na_{1/2}TiO_3$ lattices. The role of Ba and Ni cations in distortion of lattice parameters of the host $Bi_{1/2}Na_{1/2}TiO_3$ materials is shown in Fig. 3b, where the XRD patterns were enlarged in the 2θ-range of 31.0–34.0°. The XRD peaks trended to shift to lower diffraction angles which demonstrated an expansion of lattice parameters of the host $Bi_{1/2}Na_{1/2}TiO_3$ materials with the increase of the $BaNiO_{3-\delta}$ amounts. However, the satellite (012)/(110) peaks were overlapped because of the rhombohedral symmetry of the host $Bi_{1/2}Na_{1/2}TiO_3$ crystal, which makes it too hard to compare. Thus, we tried to distinguish the satellite (012)/(110) peaks via using Lorentzian fitting with an *r*-square value higher than 0.99, as shown in green and blue lines in Fig. 3b. The fitting results showed that the (012) and (110) peaks were complex distorted as depending on the $BaNiO_{3-\delta}$ amounts solid solution. Furthermore, the lattice parameters

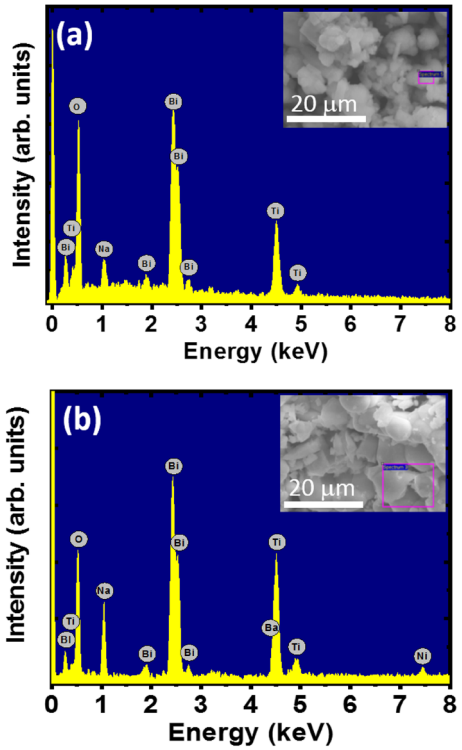

Fig. 1 EDX spectra of **a** pure $Bi_{1/2}Na_{1/2}TiO_3$ and **b** $BaNiO_{3-\delta}$-modified $Bi_{1/2}Na_{1/2}TiO_3$ materials with 5 mol.% $BaNiO_{3-\delta}$. The inset of each figure showed a selected area for chemical detection

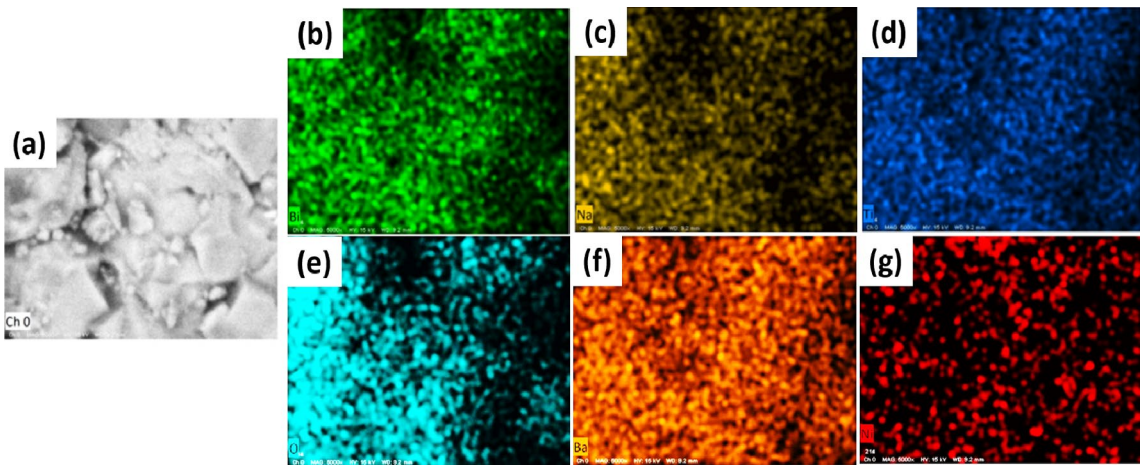

Fig. 2 **a** Image of the selected area for chemical mapping of 5 mol.% $BaNiO_{3-\delta}$-modified $Bi_{1/2}Na_{1/2}TiO_3$ material, and **b–g** chemical mappings for Bi, Na, Ti, O, Ba and Ni, respectively

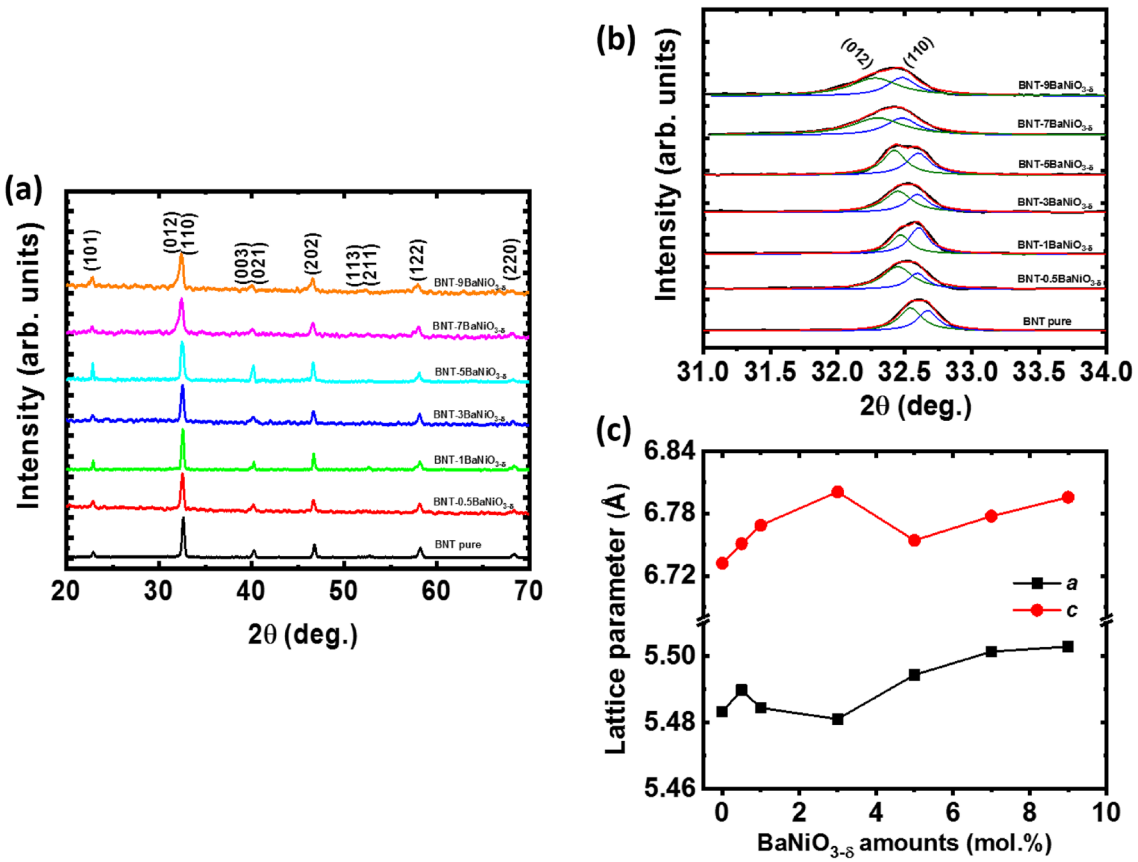

Fig. 3 **a** X-ray diffraction patterns of the pure $Bi_{1/2}Na_{1/2}TiO_3$ and $BaNiO_{3-\delta}$-modified $Bi_{1/2}Na_{1/2}TiO_3$ materials with various $BaNiO_{3-\delta}$ concentrations, **b** magnification of X-ray diffraction patterns in the 2θ-range from 31.0 to 34.0° with deconvolution of X-ray peaks, and **c** the dependence of the lattice parameters of pure $Bi_{1/2}Na_{1/2}TiO_3$ and $BaNiO_{3-\delta}$-modified $Bi_{1/2}Na_{1/2}TiO_3$ samples on the amounts of $BaNiO_{3-\delta}$ solid solution

a and *c* of the pure $Bi_{1/2}Na_{1/2}TiO_3$ and $BaNiO_{3-\delta}$-modified $Bi_{1/2}Na_{1/2}TiO_3$ as a function of $BaNiO_{3-\delta}$ amounts are shown in Fig. 3c. The figure shows that the lattice distortion is not a linear function of the $BaNiO_{3-\delta}$ concentrations in the solid solutions, which showed a complex lattice parameter distortion. The results could be explained by considering the size of impurity cations and the preferred site to be substituted. Based on Shannon's report, Bi and Na cations have a radius of 1.17 Å (in the coordination of VIII) and 1.39 Å (in the coordination of XII), respectively [29]. The radius of Ba cations (in the coordination of XII) is 1.61 Å [29]. Therefore, the substitution of Ba cations for both Bi and Na cations resulted in an expansion of lattice parameters because Ba cations are larger than Bi and Na cations. However, the difference of the valence states of Ba^{2+} impurity cations and the host cations Bi^{3+} and Na^{+} at *A*-sites in perovskite structure resulted in complex distortion where the oxygen vacancies were created via substitution of Ba^{2+} for Bi^{3+} cations, whereas the Na-vacancies were generated via incorporation of Ba^{2+} for Na^{+} cations. Oxygen vacancies, with a radius of 1.31 Å, are smaller than oxygen ions of 1.4 Å, resulting in a reduction of lattice tension, which favors a stable crystal structure [30]. The Na-vacancies also importantly decreased the stress of the lattice because Na vacancies compressed the lattice parameters [31]. In addition, the random incorporation of Ni cations into the host $Bi_{1/2}Na_{1/2}TiO_3$ materials also induced distortion of lattice parameters. The radius of Ni cations depended on their valence states and spin states [29]. Based on Shannon' report, the size of Ni^{2+} cations was 0.690 Å (at the coordination of VI); and radii of Ni^{3+} and Ni^{4+} cations at low-spin state are 0.56 Å and 0.48 Å (at the coordination of VI), respectively, while the size of Ni^{3+} with a high-spin state was 0.60 Å (at the coordination of VI) [29]. The radius of Ti^{4+} cations is 0.605 Å (at the coordination of VI) [29]. Therefore, the substitution of only Ni^{2+} cations for Ti^{4+} cations resulted in an expansion of lattice parameters; otherwise, the incorporation of other Ni cations into Ti-site resulted in a compression of lattice parameters. However, the large lattice expansion by Ba^{2+} cations incorporation with *A*-sites resulted in increasing the lattice energy of the host materials, which were possibly reduced via incorporation of Ni cations at *A*-sites with radii of 0.55 Å (at the coordination

of IV) [29, 32]. Moreover, the valence state of Ti^{4+} cations might reduce to Ti^{3+} via surrounding oxygen vacancies [33]. The reduction of the valence state from Ti^{4+} to Ti^{3+} resulted in an expansion of lattice parameters because the radii of Ti^{3+} cations of 0.670 Å at the coordination of IV are larger than those of Ti^{4+} cations of 0.605 Å at the same coordination [29]. In fact, it was difficult to separate the role of individual cation contributing to the lattice parameters of the $Bi_{1/2}Na_{1/2}TiO_3$ materials. However, the observation of lattice parameter distortion as a function of $BaNiO_{3-\delta}$ amounts was solid evidence for the random incorporation of Ba and Ni into the host lattices. In other words, the solid solutions between $Bi_{1/2}Na_{1/2}TiO_3$ and $BaNiO_{3-\delta}$ materials were well synthesized.

Figure 4a showed the Raman scattering spectra of the pure $Bi_{1/2}Na_{1/2}TiO_3$ and $BaNiO_{3-\delta}$- $Bi_{1/2}Na_{1/2}TiO_3$ materials with various $BaNiO_{3-\delta}$ concentrations at room temperature. The Raman spectra of all studied samples had a similar shape with three main overlapping humps. The overlapping in Raman scattering in $Bi_{1/2}Na_{1/2}TiO_3$ materials resulted from a random distribution of Bi and Na cations at *A*-sites in the perovskite structure [34–37]. These results were well consistent with the XRD studies where the number of XRD peaks and peak positions remained unchanged as increasing $BaNiO_{3-\delta}$ concentrations in the solid solutions. The Raman scattering peaks of $Bi_{1/2}Na_{1/2}TiO_3$ materials were hard to archive in comparing as a function of $BaNiO_{3-\delta}$ impurities. Thus, we tried to distingue the Raman scattering peaks via using the Lorentzian fitting with the *r*-square higher than 0.99. The results of the devolution of Raman scattering peaks are shown in Fig. 4b for pure $Bi_{1/2}Na_{1/2}TiO_3$ material and $BaNiO_{3-\delta}$-modified $Bi_{1/2}Na_{1/2}TiO_3$ materials. Niranjan et al. predicted that the low vibration modes in the range 109–134 cm^{-1} originated from displacements of Bi-O ions, while higher frequency in the range of 155–187 cm^{-1} was related to Na–O vibrations, whereas the TiO_6 vibration was shown in the frequency range of 246–401 cm^{-1}, while the vibration range 413–826 cm^{-1} was assigned the vibration of oxygen atoms [34]. Kreisel et al. reported that TiO6 active at 540 cm^{-1} [35]. Schutz et al. obtained that wavenumber smaller than 150 cm^{-1} was associated with the vibration of the perovskite *A*-site, and wavenumber range 150–450 cm^{-1} was associated with Ti–O vibration, especially the mode with the highest intensity of 305 cm^{-1} has been assigned as A_1 mode closely related to the strength of the Ti–O bond, where high-frequency bands above 450 cm^{-1} have been associated with TiO6 vibrations, namely the breathing and stretching modes of the oxygen octahedral, and in the range of 450–700 cm^{-1} which were three modes are observed A_1(TO) (~485 cm^{-1}), A1(LO) (~540 cm^{-1}), and overlapping E(LO) and E(TO) modes (~620 cm^{-1}) [36]. The distortion of frequency modes around 425 cm^{-1} was further suggested for distortion of Ti–O or TiO_6 vibration modes via generation of new activity vibration modes of Ti(Ni)-O or Ti(Ni)O6 cause of mass of Ni cations (~58.69 g/mol) were larger than that of Ti cations (~47.87 g/mol), which were distributed to evidence for the substitution of Ni into Ti-site of host $Bi_{1/2}Na_{1/2}TiO_3$ compounds. Based on the structure studied by XRD and Raman scattering, the results provided that the $BaNiO_{3-\delta}$ materials were well solid solute into the host $Bi_{1/2}Na_{1/2}TiO_3$ compounds.

Figure 5a showed the absorption spectra of pure $Bi_{1/2}Na_{1/2}TiO_3$ material and $BaNiO_{3-\delta}$-modified $Bi_{1/2}Na_{1/2}TiO_3$ materials with various amounts as solid solution. The single edge with slightly tails was obtained in absorption spectroscopy of pure $Bi_{1/2}Na_{1/2}TiO_3$ material, which were related to self-defect and/or surface defects [7]. The absorption edge of the pure $Bi_{1/2}Na_{1/2}TiO_3$ was estimated at 420 nm. The addition of $BaNiO_{3-\delta}$ with various amounts into host $Bi_{1/2}Na_{1/2}TiO_3$ materials resulted in titling the absorption edge to a higher wavelength and induced the hump from 600 to 820 nm. In addition, the absorption coefficient of $BaNiO_{3-\delta}$-modified $Bi_{1/2}Na_{1/2}TiO_3$ materials was lifted as increasing the $BaNiO_{3-\delta}$ concentration. The redshift in the absorption spectra of the $Bi_{1/2}Na_{1/2}TiO_3$ materials via the addition of $BaNiO_{3-\delta}$ materials was consistent

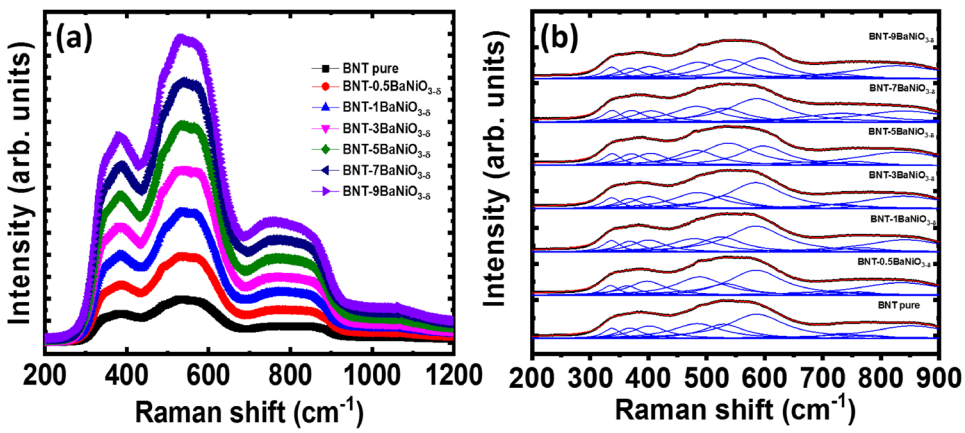

Fig. 4 **a** Raman scattering spectra and **b** deconvoluted Raman spectra of the pure $Bi_{1/2}Na_{1/2}TiO_3$ and $BaNiO_{3-\delta}$-modified $Bi_{1/2}Na_{1/2}TiO_3$ materials as a function of $BaNiO_{3-\delta}$ concentrations

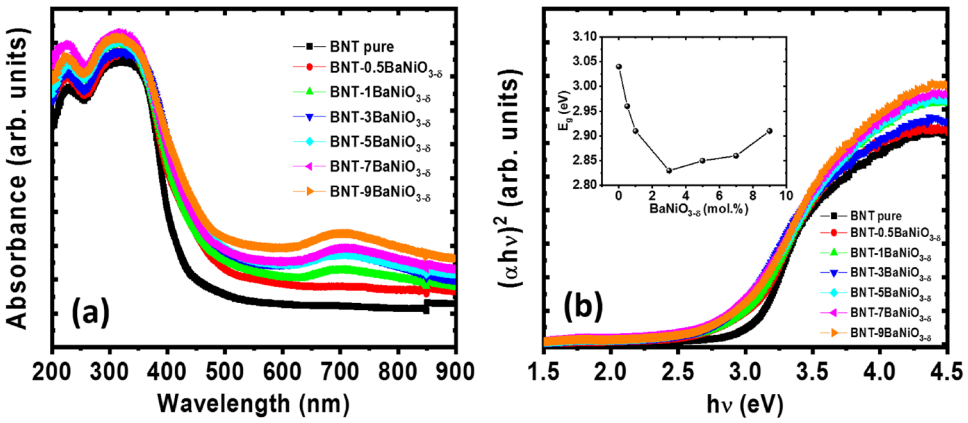

Fig. 5 **a** Absorption spectra and **b** the plotted of $(\alpha h\nu)^2$ as a function of photon energy ($h\nu$) of the pure $Bi_{1/2}Na_{1/2}TiO_3$ and $BaNiO_{3-\delta}$-modified $Bi_{1/2}Na_{1/2}TiO_3$ materials with various $BaNiO_{3-\delta}$ amounts. The inset of Fig. 5b showed the dependence of E_g values as a function of $BaNiO_{3-\delta}$ concentrations

with recent reports on host $Bi_{1/2}Na_{1/2}TiO_3$ lattices incorporated with Ni cations [12, 13, 32, 37]. The appearance of a hump in a high wavelength range via the introduction of $BaNiO_{3-\delta}$ into host $Bi_{1/2}Na_{1/2}TiO_3$ materials possibly originated from inter-transition of 3*d*–3*d* of Ni cations [32, 38]. Recently, Linh et al. predicted that $Bi_{1/2}Na_{1/2}TiO_3$ materials exhibited the direct bandgap transition [39]. Thus, the optical bandgap (E_g) of the pure $Bi_{1/2}Na_{1/2}TiO_3$ and $BaNiO_{3-\delta}$-modified $Bi_{1/2}Na_{1/2}TiO_3$ materials was roughly estimated from the Wood–Tauc method [7, 24]. To follow this method, the $(ah\nu)^2$ values were plotted as a function of photon energy ($h\nu$), as shown in Fig. 5b. The magnitudes of E_g values were calculated by extrapolating the straight-line downing to zero of the photon energy axis. The estimated E_g values were shown as a function of $BaNiO_{3-\delta}$ in the inset of Fig. 5b. The pure $Bi_{1/2}Na_{1/2}TiO_3$ exhibited the E_g value of 3.04 eV, which was consistent with recent reports on the same materials [33, 37, 38]. The E_g values decreased as increasing the $BaNiO_{3-\delta}$ concentration up to 3 mol.% solid solute in the host $Bi_{1/2}Na_{1/2}TiO_3$ materials. Further addition of $BaNiO_{3-\delta}$ into the host $Bi_{1/2}Na_{1/2}TiO_3$ materials resulted in increasing E_g up to 2.91 eV for the 9 mol.% $BaNiO_3$ solid solution. This was quite an interesting phenomenon because the value was far from recent observations on Ni-containing $Bi_{1/2}Na_{1/2}TiO_3$ materials. Pradhan et al. reported that E_g values of $Bi_{1/2}Na_{1/2}TiO_3$ materials increased from 3.20 to 3.22 eV by replacing Ti^{4+} with Ni^{2+} from creating hole states at the top of the valence band [38]. Chen et al. observed a reduction of bandgap from 2.11 to 1.98 eV as increasing $NiTiO_3$ in $NiTiO_3$-modified $Bi_{1/2}Na_{1/2}TiO_3$ materials, which was related to the random distribution of polyvalent Ni ions at the octahedral sites and/or the promotion from oxygen vacancies [32]. Recently, Dung et al. reported that the monotone reduction of the optical bandgap of $Bi_{1/2}Na_{1/2}TiO_3$ materials from 3.12 to 2.23 eV via increasing the Ni doping concentrations originated from the local electronic state of 3*d* Ni cations in the electronic band structure of $Bi_{1/2}Na_{1/2}TiO_3$ materials [12]. In this study, the observed trend of the optical bandgap of $Bi_{1/2}Na_{1/2}TiO_3$ solid solutions as a function of $BaNiO_{3-\delta}$ concentrations was involved in the contribution of complex random incorporation of Ba cations. The substitution of Ba at *A*-sites generated new local states in the electronic band structure of $Bi_{1/2}Na_{1/2}TiO_3$ materials. However, due to unbalance of valence states between Ba^{2+} impurity cations and the host (Bi^{3+} and Na^+) cations, the incorporation of Ba^{2+} cations to Bi^{3+} cations created oxygen vacancies, while the substitution of Ba^{2+} cations for Na^+ cations generated sodium vacancies. The appearance of Na and O vacancies exhibited new local states, which possibly trapped photons, resulting in a decrease of the optical bandgap of the $Bi_{1/2}Na_{1/2}TiO_3$ materials. The substitution of the large Ba cations caused considerable stress in the host $Bi_{1/2}Na_{1/2}TiO_3$ lattices that possibly tuned the optical bandgap of the host materials by modifying the electronic band structure [40]. In addition, the valence state of Ti and/or Ni cations might complexly change by decreasing the valence state of Ti^{4+} to Ti^{3+} via surrounding oxygen vacancies [33]. The high valence state of $Ni^{4+/3+}$ cations is possibly reduced via interaction with Ti^{3+} defect, e.g., $Ni^{4+/3+}+Ti^{3+} \rightarrow Ni^{3+/2+}+Ti^{4+}$, which also contributed to a new local state and/or modified electronic band structure of the host $Bi_{1/2}Na_{1/2}TiO_3$ materials via chemical strain [33, 40, 41]. Our observation provided that the E_g values of the $Bi_{1/2}Na_{1/2}TiO_3$ materials reached a minimum as increasing the $BaNiO_{3-\delta}$ amounts and trended to increase for further increasing $BaNiO_{3-\delta}$ concentrations. It was suggested that the complex change in E_g values related to Ni cations filling to the corner of octahedral as interstitial rather than substitution cause of reducing the stress of lattice and/or the replacement at *A*-sites rather than *B*-sites. In fact, at this moment, we could not show the direct evidence for Ni cations location at intestinal. However, based on the observation of E_g change as a function of $BaNiO_{3-\delta}$ concentrations, we suggested that the $BaNiO_{3-\delta}$ materials were complex solid solutes in the host $Bi_{1/2}Na_{1/2}TiO_3$ lattices.

Furthermore, the role of $BaNiO_{3-\delta}$ materials on the photoluminescence properties of $Bi_{1/2}Na_{1/2}TiO_3$ materials is shown in Fig. 6. The figure indicated that photoluminescence spectra of the pure $Bi_{1/2}Na_{1/2}TiO_3$ and $BaNiO_{3-\delta}$-modified $Bi_{1/2}Na_{1/2}TiO_3$ materials were complex which exhibited much information of charge transfer processes. The prominent PL peaks located in the range from 478 to 505 nm, as shown in the inset of Fig. 6, where the PL spectra were enlarged in the wavelength range of 478–510 nm. In addition, some PL broad peaks were observed at a higher wavelength from 510 to 850 nm. The origin of PL peaks of $Bi_{1/2}Na_{1/2}TiO_3$ materials was still unclear in the recent literature reports [7, 24, 42]. The photoluminescence of $Bi_{1/2}Na_{1/2}TiO_3$ materials tended to suppress as increasing the $BaNiO_{3-\delta}$ amounts. The PL suppression in $Bi_{1/2}Na_{1/2}TiO_3$ materials by the introduction of transition metals was well reported [7, 24]. The highest PL intensity of $Bi_{1/2}Na_{1/2}TiO_3$ materials was obtained at a wavelength around 483 nm, which was far from the observation of absorption edge of around 420 nm from the UV–vis spectra. Thus, we suggested that the main PL peaks came from other phenomena than band-to-band charge transitions. Unlike oxide materials, $Bi_{1/2}Na_{1/2}TiO_3$ materials are ferromagnetic oxides that exhibited the ferroelectric domain as remanent electrical polarization [42]. Therefore, the PL processes of lead-free ferroelectric $Bi_{1/2}Na_{1/2}TiO_3$ materials are mostly related to a charge transfer process at surfaces because the cations at the surface normally have many un-bonding pairs [43]. Recently, the PL peaks of lead-free ferroelectric Bi-based materials were suggested to originate from the tilt of TiO6-TiO6 adjacent octahedra, resulting in the generation of localized electron levels above the valence band [44]. Thus, the suppression of PL intensity of $Bi_{1/2}Na_{1/2}TiO_3$ materials as increasing the addition of $BaNiO_{3-\delta}$ amounts was suggested to result from the absorption of photon generated from hole–electron recombination via defects such as Ba and Ni cations. In other words, the suppression of photoluminescent of $Bi_{1/2}Na_{1/2}TiO_3$ materials via addition of $BaNiO_{3-\delta}$ as impurities solid solution was provided solid evidence for random incorporate of Ba and Ni into host lattice of $Bi_{1/2}Na_{1/2}TiO_3$ materials.

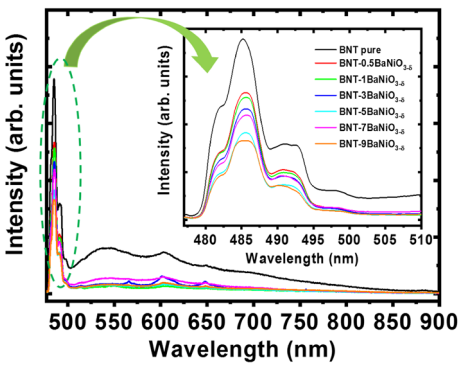

Fig. 6 Photoluminescent spectra of pure $Bi_{1/2}Na_{1/2}TiO_3$ material and $BaNiO_{3-\delta}$-modified $Bi_{1/2}Na_{1/2}TiO_3$ materials with various $BaNiO_{3-\delta}$ amounts. The inset of the figure showed magnification of photoluminescent spectra in the wavelength range of 478–510 nm

Figure 7 showed the magnetization as a function of the applied magnetic field, M-H curves, at room temperature for the pure $Bi_{1/2}Na_{1/2}TiO_3$ and $BaNiO_{3-\delta}$-modified $Bi_{1/2}Na_{1/2}TiO_3$ materials with various $BaNiO_{3-\delta}$ concentrations. As shown in Fig. 7a, the M-H curve of the pure $Bi_{1/2}Na_{1/2}TiO_3$ material exhibited an anti-*S*-shape which resulted from a compensation between the diamagnetic and weak-ferromagnetic components. The diamagnetic properties of the $Bi_{1/2}Na_{1/2}TiO_3$ materials originated from an empty 3*d*-orbital state of Ti cations, while the weak-ferromagnetism raised from vacancies such as Na, Bi, or Ti [6–8]. The diamagnetic signal of $Bi_{1/2}Na_{1/2}TiO_3$ materials tended to be suppressed via inducing the ferromagnetic signal as $BaNiO_{3-\delta}$ adding as shown in Fig. 7b–e for 0.5; 1; 3 and 5 mol.% $BaNiO_{3-\delta}$-modified $Bi_{1/2}Na_{1/2}TiO_3$ materials, respectively. Further addition of $BaNiO_{3-\delta}$ with 7 and 9 mol.% concentrations into the host $Bi_{1/2}Na_{1/2}TiO_3$ materials, M-H curves showed in unsaturation with an applied magnetic field, as shown in Fig. 7f and g, respectively. Note that all possible compound of deficiency $BaNiO_{3-\delta}$ materials was shown paramagnetic or below temperature magnetic ordering [45–47]. Takeda et al. reported that $BaNiO_3$ exhibited diamagnetic properties [45]. Lander et al. reported that $BaNiO_3$ and $Ba_2Ni_2O_5$ materials exhibited the Curie–Weiss temperatures of 210 K and 100 K, respectively [46]. By a neutron scattering study, Matsuda et al. indicated that $BaNiO_2$ had a nonmagnetic ground state and paramagnetic properties [47]. In addition, other possible clusters such as $NaNiO_{3-\delta}$ or $NiTiO_3$ materials had a low-temperature antiferromagnetic order, e.g., $NaNiO_2$ and $NiTiO_3$ with Neel temperatures of 19.5 K and 22 K, respectively [48, 49]. Therefore, the observation of weak-ferromagnetism in $BaNiO_{3-\delta}$-modified $Bi_{1/2}Na_{1/2}TiO_3$ materials was suggested as a result of the random incorporation of Ba and Ni into the host lattice, as expected to intrinsic ferromagnetism. Ba cations could substitute for both Na and Bi-sites, generating oxygen vacancies or Na vacancies, respectively: (i) the oxygen vacancies were created when Ba cations filled to Bi-sites, (ii) while Na-vacancies were generated if Ba cations substituted for Na-sites. The Na vacancies directly induced non-zero magnetic moments, while the oxygen vacancies did not show any magnetic moment [7]. However, the oxygen vacancies indirectly induced magnetic moment via promoting the valence transition from Ti^{4+} to Ti^{3+} [7, 33]. The complexity of Ni valence states might be induced by interacting with the nearest Ti^{3+} defects via equations $Ni^{4+}+Ti^{3+} \rightarrow Ni^{3+}+Ti^{4+}$ and/or $Ni^{3+}+Ti^{3+} \rightarrow Ni^{2+}+Ti^{4+}$ [33, 41]. The charge transfer between Ni impurities and Ti

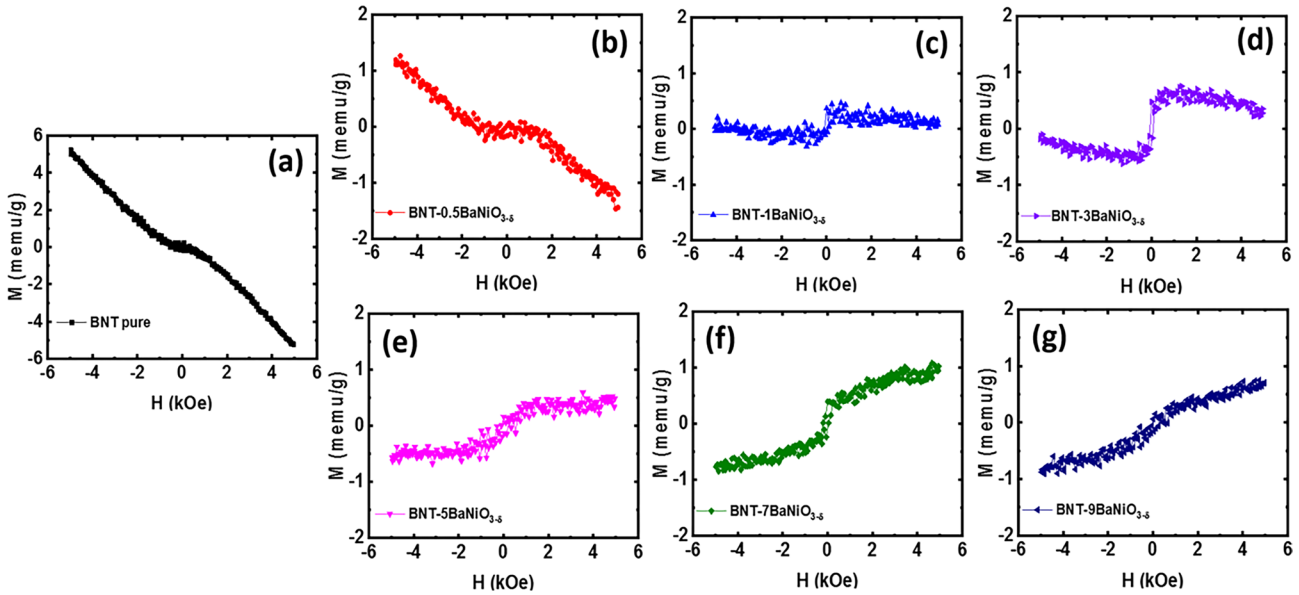

Fig. 7 M-H curves at room temperature of **a** the pure $Bi_{1/2}Na_{1/2}TiO_3$, and $BaNiO_{3-\delta}$-modified $Bi_{1/2}Na_{1/2}TiO_3$ materials with **b** 0.5 mol.%, **c** 1 mol.%, **d** 3 mol.%, **e** 5 mol.%, **f** 7 mol.% and **g** 9 mol.% of $BaNiO_{3-\delta}$

cations was recently predicted by a first-principle theoretical study [12]. Note that the momentum spin of Ni^{2+} cations was 1 μ_B/Ni, and of Ni^{3+} cations are 0.5 μ_B/Ni and 1.5 μ_B/Ni for the low-spin (LS) and high-spin (HS) configurations, respectively, while the Ni^{4+} cations had no magnet moment. Therefore, a change in the Ni valence states led to a change in the magnetic moment of pairs such as $Ni^{3+/2+}$ through

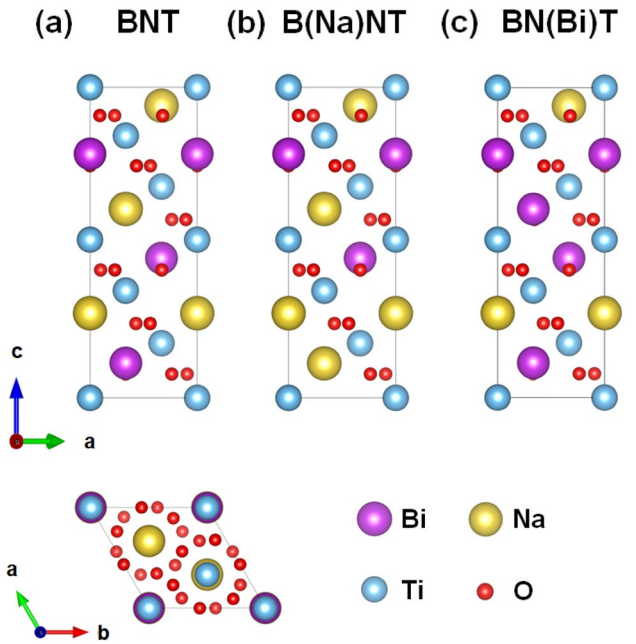

Fig. 8 Side and top views of the optimized atomic structure of **a** $Bi_{1/2}Na_{1/2}TiO_3$ (BNT), **b** Bi-site Na [B(Na)NT], and **c** Na-site Bi [BN(Bi)T] substituted BNT. The symbol for each element is indicated at the bottom

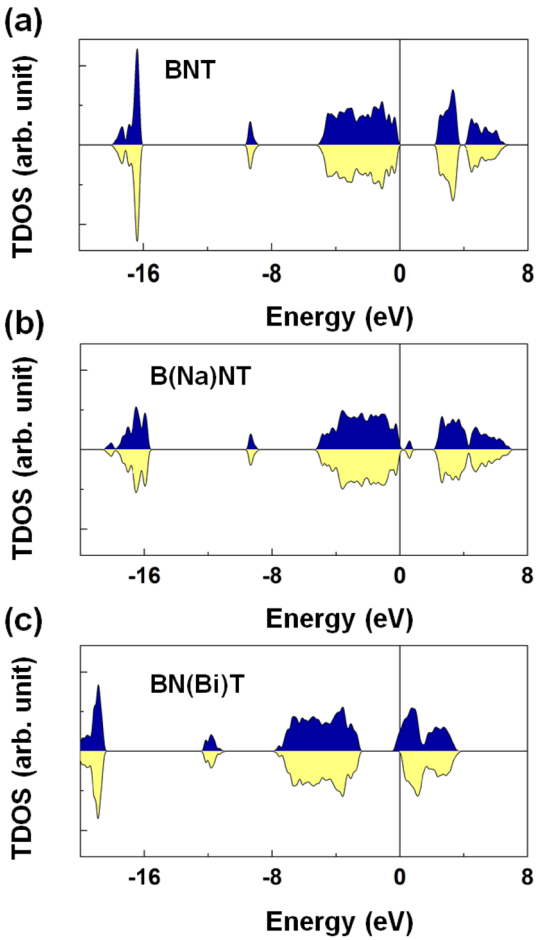

Fig. 9 DFT results of the spin-resolved total density of states (TDOS) of **a** BNT, **b** B(Na)NT, and **c** BN(Bi)T. The Fermi level is set to zero energy

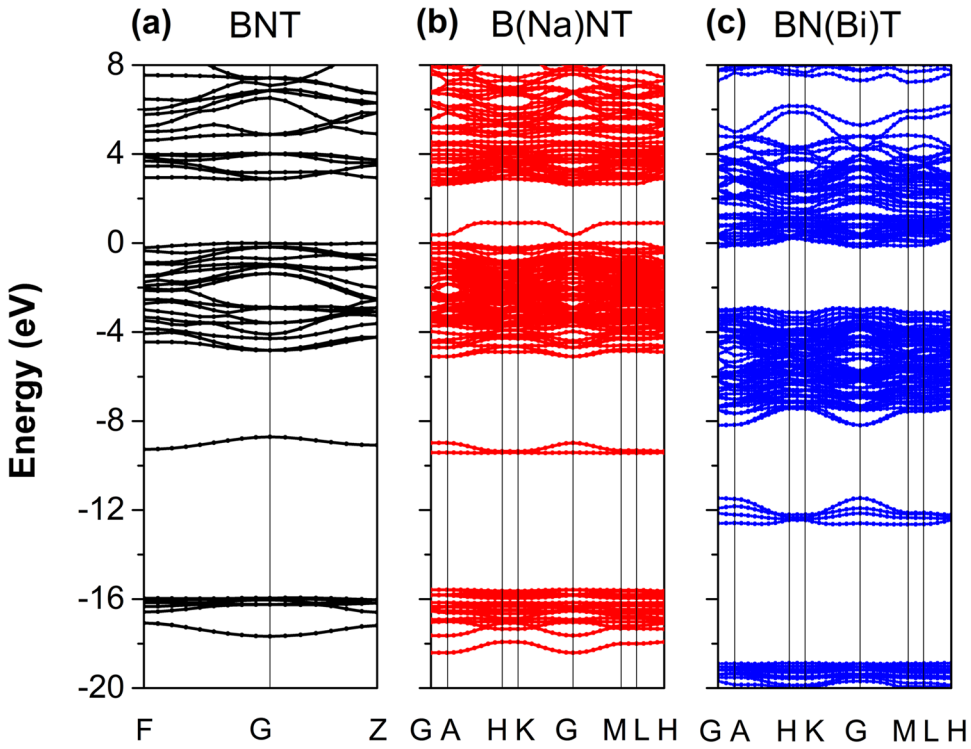

Fig. 10 DFT results of the band structures of **a** BNT, **b** B(Na)NT, and **c** BN(Bi)T. The Fermi level is set to zero energy

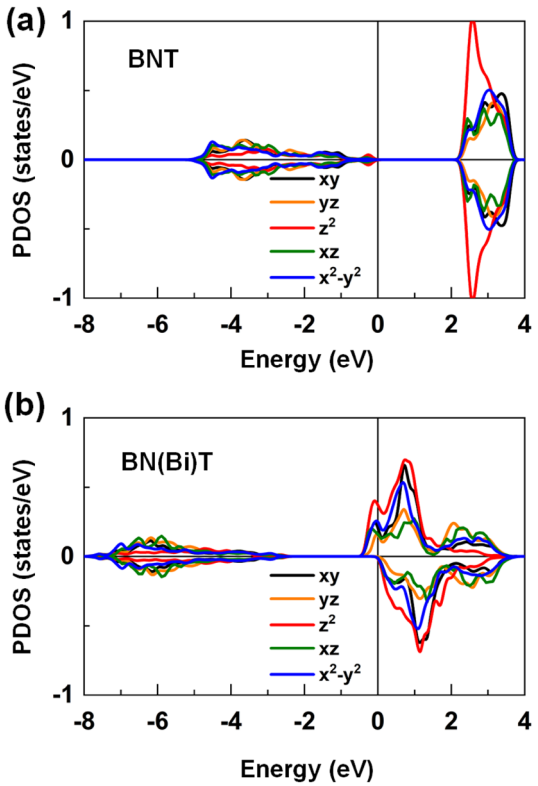

Fig. 11 The DFT results of the *d*-orbital projected density of states (PDOS) of the Ti atom for **a** BNT and **b** BN(Bi)T. The black, orange, red, green, and blue lines represent the d_{xy}, d_{yz}, d_z^2, d_{xz}, and $d_{x^2-y^2}$ orbital states, respectively. The Fermi level is set to zero energy

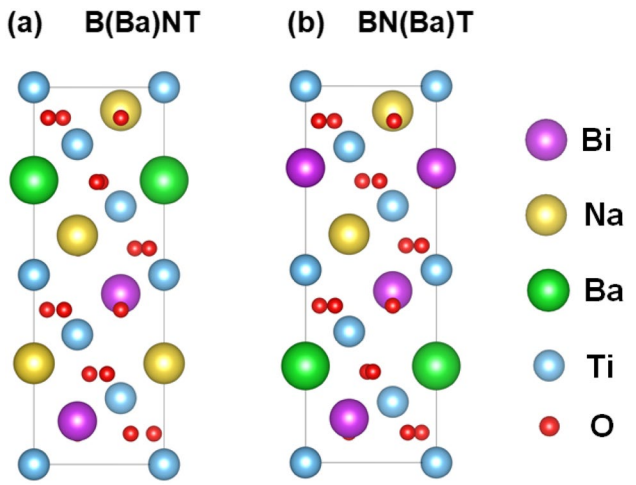

Fig. 12 Side views of the optimized atomic structures of the **a** Bi-site Ba [B(Ba)NT] and **b** Na-site Ba [BN(Ba)T] substituted $Bi_{1/2}Na_{1/2}TiO_3$ materials. The atomic symbols follow the same convention used in Fig. 8. Green spheres are the Ba substitutional atoms

oxygen vacancies (□), e.g., Ni^{3+}-□-Ni^{3+}, Ni^{2+}-□-Ni^{2+} or mixing Ni^{2+}-□-Ni^{3+}, resulting in complex magnetic ordering. The isolate of Ni cations distribution in host lattice $Bi_{1/2}Na_{1/2}TiO_3$ materials exhibited the paramagnetic signal. In addition, the unsaturation of magnetic moments of $Bi_{1/2}Na_{1/2}TiO_3$ materials for highly $BaNiO_{3-\delta}$ dopants concentration was also suggested to relate with the pair interaction of $Ni^{2+/3+}$-□-$Ni^{2+/3+}$ versus $Ni^{2+/3+}$-□-$Ni^{2+/3+}$ via

polaron modes where the antiferromagnetic-like were normally ordering [12, 13, 37]. However, unlike the single Ni cation dopants in lead-free ferroelectric materials, the magnetic moments of $BaNiO_{3-\delta}$-modified $Bi_{1/2}Na_{1/2}TiO_3$ materials were small. Therefore, we suggested that the magnetic moment of Ni cations was quenched via co-incorporation with Ba cations into host lattice $Bi_{1/2}Na_{1/2}TiO_3$ materials. That issue was possibly understood via considering two important things that Ni cations possibly filled to *A*-sites, and Ni cations occurred at the corner of octahedral as interstitial sites because the size of Ba cations was too large to compare with Bi and Na radius, resulting in large stress in crystal structural.

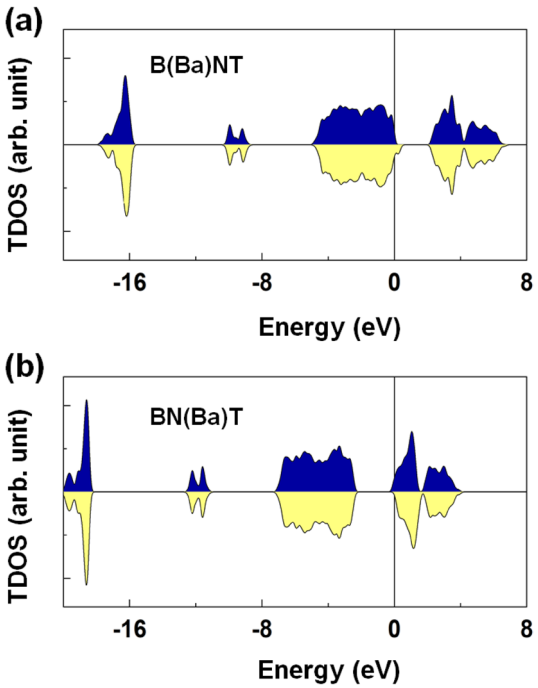

Fig. 13 The DFT results of the spin-resolved total density of states (TDOS) of **a** B(Ba)NT and **b** BN(Ba)T. The Fermi level is set to zero energy

To understand the origin of the observed ferromagnetism in $BaNiO_{3-\delta}$-modified $Bi_{1/2}Na_{1/2}TiO_3$, the DFT calculations were further performed using the Vienna ab initio simulation package (VASP) [50, 51] version 5.4.4. For the exchange–correlation potential, we adopt the generalized gradient approximation (GGA) formulated by Perdew, Burke, and Ernzerhof (PBE) [52]. We have first explored the intrinsic disordering effects between the Bi and Na sites in $Bi_{1/2}Na_{1/2}TiO_3$. The model atomic structures of the fully ordered and disordered $Bi_{1/2}Na_{1/2}TiO_3$ (BNT) are shown in Fig. 8a–c. For the disordered structure, 1 Bi (Na) atom is replaced by the Na (Bi), which we denoted as B(Na)NT [BN(Bi)T]. For all systems in this study, we used a cutoff energy of 500 eV for the plane-wave basis and a *k*-point mesh of 7×7×5 for the Brillouin zone integration. To obtain optimized atomic structures, the atomic positions and lattice parameters were fully relaxed until the largest force became less than 10^{-2} eV/Å and the change in the total energy between two ionic relaxation steps was smaller than 10^{-5} eV.

Figure 9a, b, and c present the spin-resolved total density of states (TDOS) of BNT, B(Na)NT, and BN(Bi)T compounds, respectively. For the fully ordered BNT, the valence and conduction bands were characterized by the O-2*p* and Ti-3*d* orbital

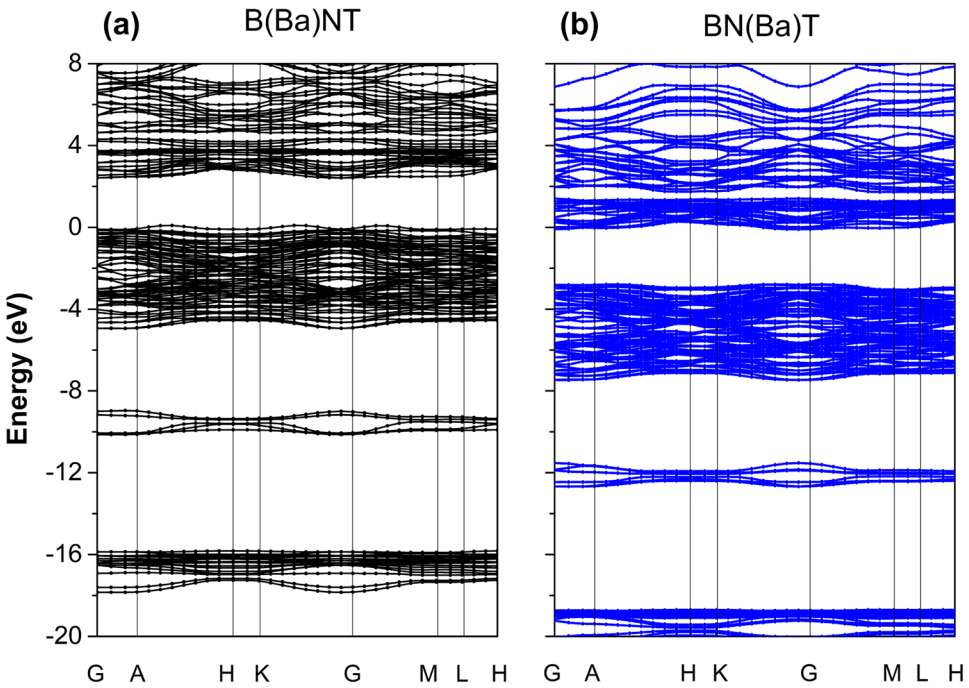

Fig. 14 The DFT results of the band structures of **a** B(Ba)NT and **b** BN(Ba)T. The Fermi level is set to zero energy

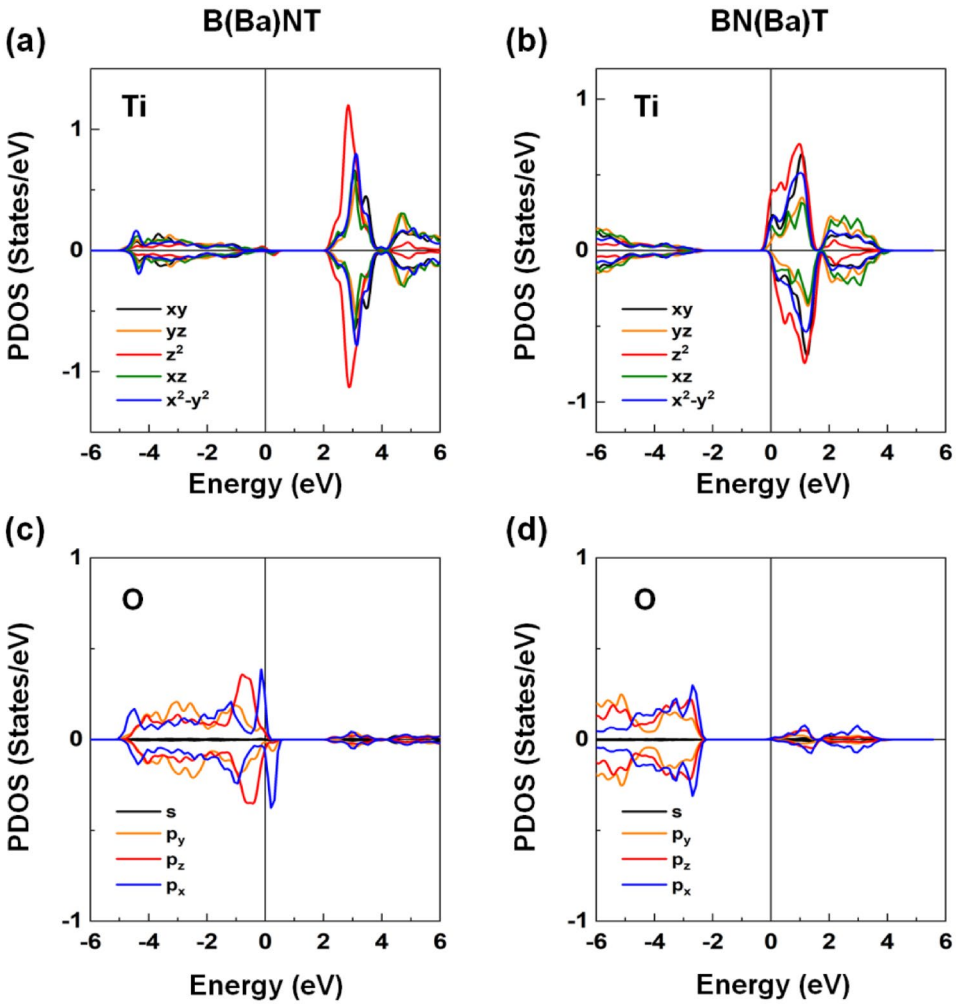

Fig. 15 The DFT results of the *d*-orbital projected density of states (PDOS) of the Ti atom of **a** B(Ba)NT and **b** BN(Ba)T. The black, orange, red, green, and blue lines represent the d_{xy}, d_{yz}, d_z^2, d_{xz}, and $d_{x^2-y^2}$ orbital states, respectively. The corresponding PDOS of the neighboring O atoms is shown at the bottom panels, respectively. The black, orange, red, and blue lines represent the *s*, p_x, p_z, and p_y orbital states, respectively. The Fermi level is set to zero energy

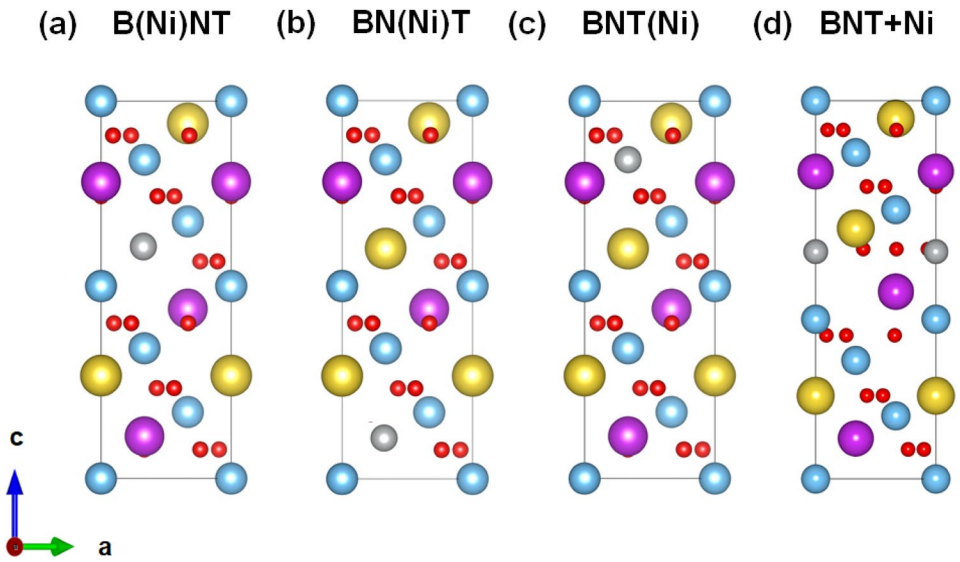

Fig. 16 Side views of the optimized atomic structures of the **a** Bi-site [B(Ni)NT], **b** Na-site [BN(Ni)T], and **c** Ti-site Ni [BNT(Ni)] substituted $Bi_{1/2}Na_{1/2}TiO_3$. **d** The same for $Bi_{1/2}Na_{1/2}TiO_3$ with an interstitial Ni. The atomic symbols follow the same convention used in Fig. 8. Gray spheres are the Ni dopant atoms

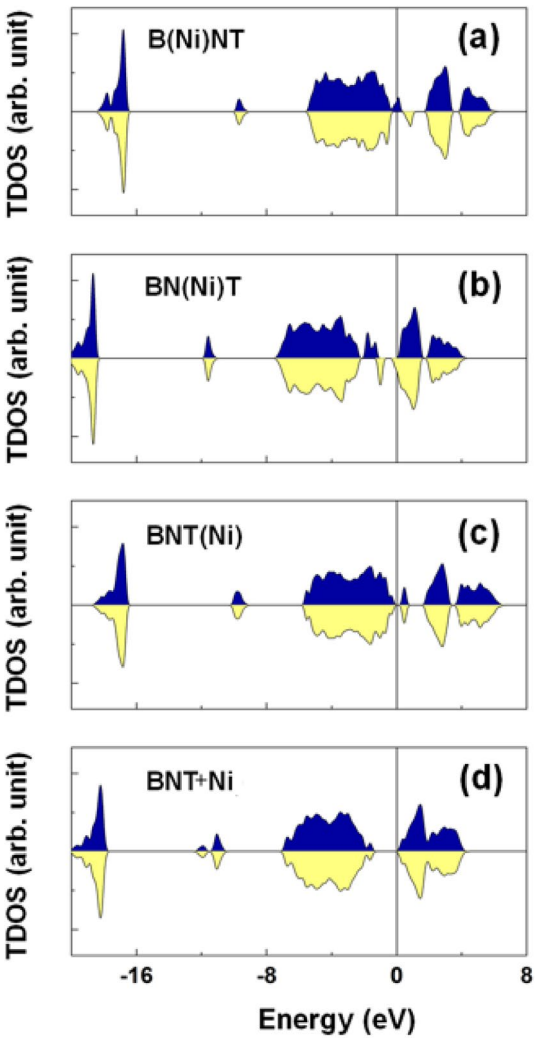

Fig. 17 The DFT results of the spin-resolved total density of states (TDOS) of **a** B(Ni)NT, **b** BN(Ni)T, **c** BNT(Ni), and **d** BNT + Ni. The Fermi level is set to zero energy

states with a bandgap of ~2.25 eV, respectively. The calculated band structures in Fig. 10a indicated that BNT had a direct bandgap; the direct transition from the minimal-energy state in the conduction band and the maximal-energy state in the valence band happened at the gamma point G in the Brillouin zone. Figure 9a shows that the majority- and minority-spin states were entirely degenerated, indicating a feature of a non-magnetic ground state of the fully ordered BNT. The calculated bandgap of BNT is smaller than the measured value (3.04 eV), which is indeed quite typical in DFT calculations for oxide perovskites [53, 54]. As shown in Fig. 9b, there is a mid-gap state in B(Na)NT-TDOS due to the electron deficit in the unit cell, which is also apparent in the band structure shown in Fig. 10b. On the other hand, for BN(Bi)T, the empty states shift toward the Fermi level, and the minimum of the conduction bands touches the Fermi level, as indicated in Fig. 10c. In particular, the unoccupied majority-spin states are partially occupied. As the spin channels split, the BN(Bi)T has an induced magnetic moment of about 1.2 μ_B per unit cell (u.c.) (or 1 Na-site Bi), which is due to the different valence states (2 electrons) of Bi^{3+} and Na^{+}. As a result, the Ti atom neighboring the Na-site Bi accumulates some charges in the majority-spin state, as shown in the *d*-orbital projected DOS (PDOS) in Fig. 11.

Next, we investigated the external impurity effects on magnetism with the $BaNiO_3$ dopants. There are two possible substitution dopant sites, *A*- and *B*-sites. For the *A*-site dopant, we replace one Bi atom and one Na atom with Ba atoms [denoted as B(Ba)NT and BN(Ba)T], as illustrated in Fig. 12a and b, respectively. Both B(Ba)NT and BN(Ba)T exhibit the magnetic ground states, where the total magnetization is 0.93 μ_B/u.c. for B(Ba)NT and 0.81 μ_B/u.c. for BN(Bi)T. These induced magnetic moments mainly come from the Ti and O atoms neighbored to the Ba substitute atoms, as revealed from the TDOS in Fig. 13 and the band structure in Fig. 14 and the PDOS analyses in Fig. 15. Figure 14a indicates that the substitution of Ba into the Bi site leads to insignificant changes in band structures of B(Ba)NT. In contrast, for BN(Ba)T, the Fermi level touches the minimum of the conduction bands, as shown in Fig. 14b.

The other possible dopant can also involve the Ni substitute atoms, which may occupy both the *A*- and *B*-sites. Accordingly, we replace one Ni atom for each Bi, Na, and Ti site, as shown in Fig. 16a–c, respectively. In Fig. 16d, we also consider the interstitial Ni dopant in the unit cell, in line with our experimental finding. Here, they are denoted as B(Ni)NT, BN(Ni)T, BNT(Ni), and BNT + Ni, respectively. The TDOS has shown in Fig. 17 indicates that the former two, B(Ni)NT and BN(Ni)T, prefer the magnetic nature, whereas the latter two, BNT(Ni) and BNT + Ni, are still nonmagnetic. The band structures in Fig. 18a–d indicate that the substitution of Ni for all sites creates the mid-gap energy levels. From more detailed analyses with the PDOS in Fig. 17 and the spin density map in Fig. 19, it is obvious that the magnetism arises at the Ni dopant site as Ni is one of the magnetic elements in nature. The calculated local magnetic moments of the Ni atom are 0.75 and 1.23 μ_B for B(Ni)NT and BN(Ni)T, respectively. There is a slight distribution of the spin density over the neighboring O atoms in B(Ni)NT (Fig. 19a and Fig. 20) and the neighboring Ti and O atoms around the Ni in BN(Ni)T (Fig. 19b). For the latter, the valence state of Ti^{4+} tends to change to Ti^{3+} due to the spin-polarized charge transfer from the Na-site Ni atom because the Ni has more valence than the Na.

4 Conclusions

The $BaNiO_{3-\delta}$-addition $Bi_{1/2}Na_{1/2}TiO_3$ materials as solid solutions were synthesized by sol–gel method and investigated by first-principles calculations for electronic structure

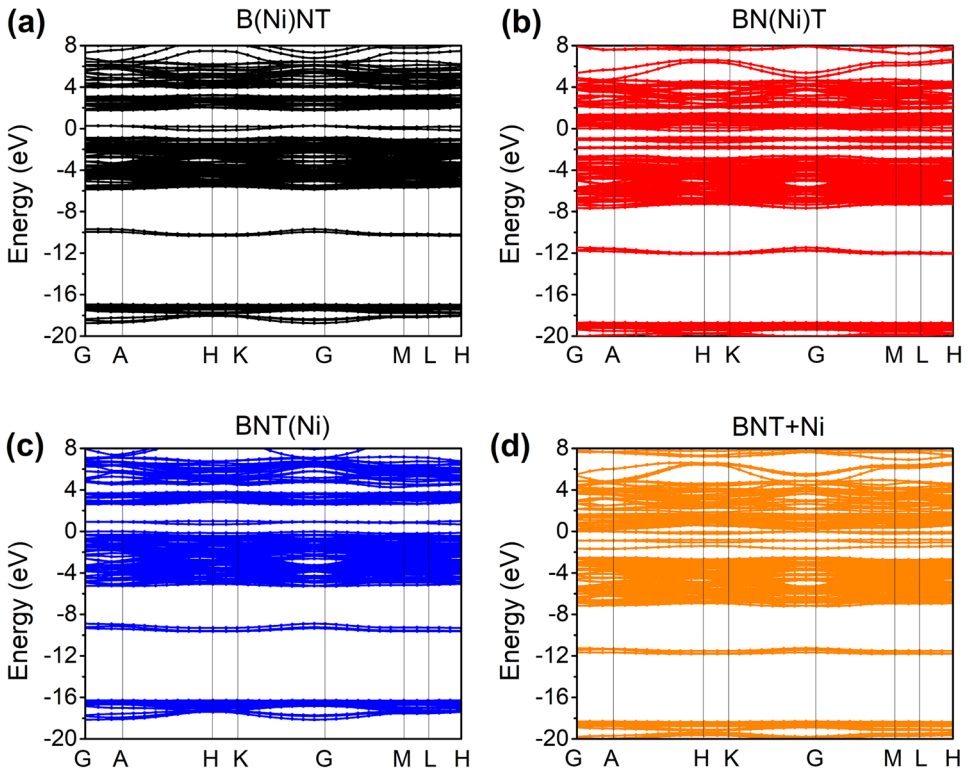

Fig. 18 The DFT results of the band structures of **a** B(Ni)NT, **b** BN(Ni)T, **c** BNT(Ni), and **d** BNT+Ni. The Fermi level is set to zero energy

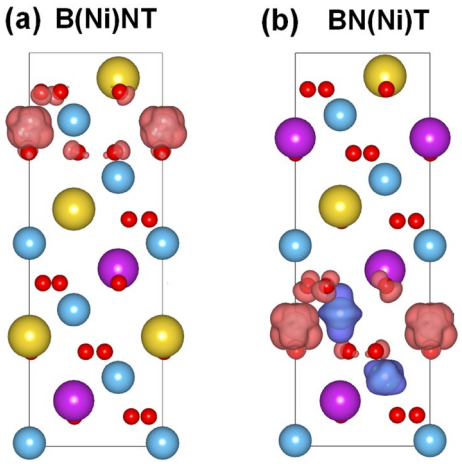

Fig. 19 The DFT result of the spin density of a B(Ni)NT and b BN(Ni)T. Red and blue isosurfaces represent the spin-up and spin-down states, respectively. The atomic symbols follow the same convention used in Fig. 8

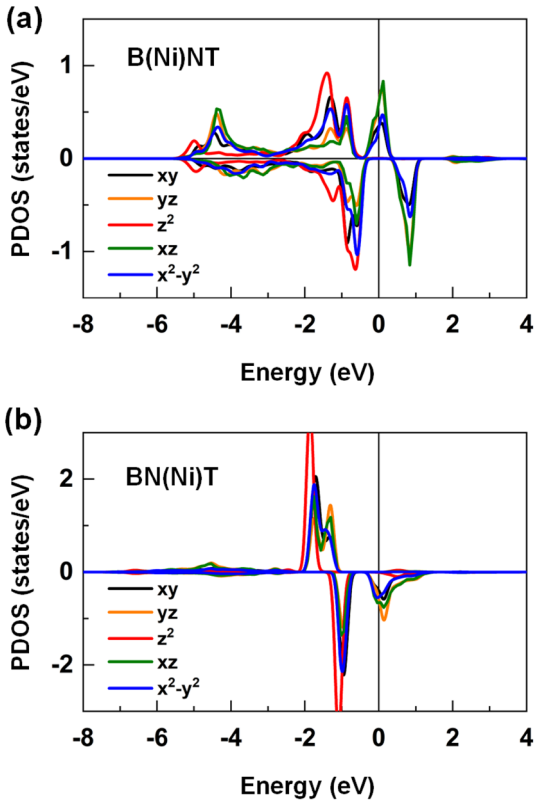

Fig. 20 The DFT results of the *d*-orbital projected density of states (PDOS) of the Ni dopant atom for **a** B(Ni)NT and **b** BN(Ni)T. The black, orange, red, green, and blue lines represent the d_{xy}, d_{yz}, d_z^2, d_{xz}, and $d_{x^2-y^2}$ orbital states, respectively. The Fermi level is set to zero energy

analyses. The substitution of Ba and Ni cations in the host lattice $Bi_{1/2}Na_{1/2}TiO_3$ materials resulted in a modification of the optical bandgap and suppression of the photoluminescence. The complex magnetic properties of $Bi_{1/2}Na_{1/2}TiO_3$ materials were obtained as a function multi-incorporation of Ba and Ni cations into host lattice. We expected that our work would importantly contribute to a birth-eye view in

the current injection of ferromagnetic properties in lead-free ferroelectric materials for smart electronic applications.

Acknowledgements This research is funded by Vietnam National Foundation for Science and Technology Development Vietnam (NAFOSTED) under grant number 103.02-2019.366. This work is supported by the Incheon National University Research Grant No. 20180438. This research was partially supported by the Nippon Sheet Glass Foundation.

Ethical approval The authors declare that they have no known competing financial interests or personal relationships that could have appeared to influence the work reported in this paper. The authors declare that this manuscript is original, has not been published before, and is not currently being considered for publication elsewhere. The authors can confirm that the manuscript has been read and approved by all named authors and that there are no other persons who satisfied the criteria for authorship but are not listed. The authors further confirm that the order of authors listed in the manuscript has been approved by all of us.

References

1. N.A. Spaldin, R. Ramesh, Nature Mater. **18**, 203–212 (2019)
2. S. Shevlin, Nature Mater. **18**, 191–192 (2018)
3. N.A. Spaldin, Proc. R. Soc. A **476**, 20190542 (2020)
4. N.D. Quan, L.H. Bac, D.V. Thiet, V.N. Hung, D.D. Dung, Adv. Mater. Sci. Eng. **2014**, 365391 (2014)
5. G.A. Smolensky, V.A. Isupov, A.I. Agranovskaya, N.N. Krainic, J. Sov. Phys. Solid State **2**, 2651–2654 (1961)
6. L. Ju, C. Shi, L. Sun, Y. Zhang, H. Qin, J. Hu, J. Appl. Phys. **116**, 083909 (2014)
7. N.T. Hung, N.H. Lam, A.D. Nguyen, L.H. Bac, N.N. Trung, D.D. Dung, Y.S. Kim, N. Tsogbadrakh, T. Ochirkhuyag, D. Odkhuu, Sci. Rep. **10**, 6189 (2020)
8. L.T.H. Thanh, N.B. Doan, N.Q. Dung, L.V. Cuong, L.H. Bac, N.A. Duc, P.Q. Bao, D.D. Dung, J. Electron. Mater. **46**, 3367–3372 (2017)
9. L.T.H. Thanh, N.B. Doan, L.H. Bac, D.V. Thiet, S. Cho, P.Q. Bao, D.D. Dung, Mater. Lett. **186**, 239–242 (2017)
10. D.D. Dung, N.B. Doan, N.Q. Dung, N.H. Linh, L.H. Bac, L.T.H. Thanh, N.N. Trung, N.V. Duc, L.V. Cuong, D.V. Thiet, S. Cho, J. Supercond. Novel Magn. **32**, 3011–3018 (2019)
11. D.D. Dung, N.B. Doan, N.Q. Dung, L.H. Bac, N.H. Linh, L.T.H. Thanh, D.V. Thiet, N.N. Trung, N.C. Khang, T.V. Trung, N.V. Duc, J. Sci. Adv. Mater. Dev. **4**, 584–590 (2019)
12. D.D. Dung, N.Q. Dung, N.B. Doan, N.H. Linh, L.H. Bac, N.N. Trung, N.V. Duc, L.T.H. Thanh, L.V. Cuong, D.V. Thiet, S. Cho, J. Supercond. Novel Magn. **33**, 911–920 (2020)
13. M.M. Hue, N.Q. Dung, N.N. Trung, L.H. Bac, L.T.K. Phuong, N.V. Duc, D.D. Dung, Appl. Phys. A **124**, 588 (2018)
14. M.M. Hue, N.Q. Dung, L.T.K. Phuong, N.N. Trung, N.V. Duc, L.H. Bac, D.D. Dung, J. Magn. Magn. Mater. **471**, 164–168 (2019)
15. D.D. Dung, N.Q. Dung, M.M. Hue, N.H. Lam, L.H. Bac, L.T.K. Phuong, N.N. Trung, D.D. Tuan, N.D. Quan, D. Sangaa, D. Odkhuu, Vacuum **179**, 109551 (2020)
16. D.D. Dung, M.M. Hue, N.Q. Dung, N.H. Lam, L.T.K. Phuong, L.H. Bac, N.N. Trung, N.V. Duc, D. Odkhuu, J. Electroceram. **44**, 129–135 (2020)
17. D.D. Dung, N.T. Hung, Appl. Phys. A **126**, 240 (2020)
18. D.D. Dung, N.T. Hung, J. Supercond. Novel Magn. **33**, 1249–1256 (2020)
19. D.D. Dung, N.T. Hung, J. Electron. Mater. **49**, 5317–5325 (2020)
20. N.T. Hung, L.H. Bac, N.N. Trung, N.T. Hoang, P.V. Vinh, D.D. Dung, J. Magn. Magn. Mater. **451**, 183–186 (2018)
21. N.T. Hung, L.H. Bac, N.T. Hoang, P.V. Vinh, N.N. Trung, D.D. Dung, Physica B **531**, 75–78 (2018)
22. D.D. Dung, N.T. Hung, D. Odkhuu, J Magn. Magn. Mater. **482**, 31–37 (2019)
23. D.D. Dung, N.T. Hung, D. Odkhuu, Appl. Phys. A **125**, 465 (2019)
24. D.D. Dung, N.T. Hung, D. Odkhuu, Sci. Rep. **3**, 18186 (2019)
25. J.G. Lee, H.J. Hwang, O. Kwon, O.S. Jeon, J. Jang, Y.G. Shul, Chem. Commun. **52**, 10731–10734 (2016)
26. R. Gottschall, R. Schollhorn, M. Muhler, N. Jansen, D. Walcher, P. Gutlich, Inorg. Chem. **37**, 1513–1518 (1998)
27. A.M.A. Lopez, M. Huve, P. Simon, O. Mentre, Chem. Commun. **55**, 3717–3720 (2019)
28. J.J. Lander, Acta Cryst. **4**, 148–156 (1951)
29. R.D. Shannon, Acta Cryst. A **32**, 751–767 (1976)
30. C. Chatzichristodoulou, P. Norby, P.V. Hendriksen, M.B. Mogensen, J. Electroceram. **34**, 100–107 (2015)
31. I.K. Jeong, Y.S. Sung, T.K. Song, M.H. Kim, A. Llobet, J. Korean Phys. Soc. **67**, 1583–1587 (2015)
32. Z. Chen, C. Yuan, X. Liu, L. Meng, S. Cheng, J. Xu, C. Zhou, J. Wang, G. Rao, Mater. Sci. Semicond. Proc. **115**, 105089 (2020)
33. X. Liu, H. Fan, J. Shi, L. Wang, H. Du, RSC Adv. **6**, 30623–30627 (2016)
34. M.K. Niranjan, T. Karthik, S. Asthana, J. Pan, U.V. Waghmare, J. Appl. Phys. **113**, 194106 (2013)
35. J. Kreisel, A.M. Glazer, J. Phys. Condens. Matter. **12**, 9689–9698 (2000)
36. D. Schutz, M. Deluca, W. Krauss, A. Feteira, T. Jackson, K. Reichmann, Adv. Func. Mater. **22**, 2285–2294 (2012)
37. D.D. Dung, M.M. Hue, N.Q. Dung, L.T.K. Phuong, L.H. Bac, N.X. Duong, P.D. Luong, N.A. Duc, N.N. Trung, N.H. Thoan, D. Odkhuu, Vacuum **177**, 109306 (2020)
38. S.K. Pradhan, S.K. De, Ceram. Inter. **44**, 15181–15191 (2018)
39. N.H. Linh, N.H. Tuan, D.D. Dung, P.Q. Bao, B.T. Cong, L.T.H. Thanh, J. Sci. Adv. Mater. Dev. **4**, 492–498 (2019)
40. C. Kittel, *Introduction to solid state physics* (8th edn) (Wiley, 2004), pp. 187–190.
41. V. Schmitt, F. Raether, J. European Ceram. Soc. **34**, 15–21 (2014)
42. J. Yin, H. Tao, G. Liu, J. Wu, J. American Ceram. Soc. **103**, 1881–1890 (2020)
43. Y. Lin, C.W. Nan, J. Wang, H. He, J. Zhai, L. Jiang, Mater. Lett. **58**, 829–832 (2004)
44. L.H. Bac, L.T.H. Thanh, N.V. Chinh, N.T. Khoa, D.V. Thiet, T.V. Trung, D.D. Dung, Mater. Lett. **164**, 631–635 (2016)
45. Y. Takeda, M. Shimada, F. Kanamaru, M. Koizumi, Chem. Lett. **3**, 107–108 (1974)
46. J.J. Lander, L.A. Wooten, J. American Chem. Soc. **73**, 2452–2454 (1951)
47. M. Matsuda, K. Katsumata, A. Zheludev, S.M. Shapiro, G. Shirane, J. Phys. Chem. Solids **60**, 1121–1123 (1999)
48. P.J. Baker, T. Lancaster, S.K. Blundell, M.L. Brooks, W. Hayes, D. Prabhakaran, F.L. Pratt, Phys. Rev. B **72**, 104414 (2005)
49. G.S. Heller, J.J. Stickler, S. Kern, A. Wold, J. Appl. Phys. **34**, 1033 (1963)
50. G. Kresse, J. Hafner, Phys. Rev. B **47**, 558 (1993)
51. G. Kresse, J. Furthmuller, Phys. Rev. B **54**, 11169 (1996)
52. J.P. Perdew, K. Burke, M. Ernzerhof, Phys. Rev. Lett. **77**, 3865 (1996)
53. J. Padilla, D. Vanderbilt, Phys Rev B **56**, 1625 (1997)
54. D.D. Dung, N.H. Lam, A.D. Nguyen, N.N. Trung, N.V. Duc, N.T. Hung, Y.S. Kim, D. Odkhuu, Sci. Rep. **11**, 8908 (2021)